Extraction of Antarctic ice features using hybrid polarimetric RISAT-1 SAR data

Esha Shah[1,*], P. Jayaprasad[2], Raghav Mehra[2], Deepak Putrevu[2], Arundhati Misra[2] and M. E. James[1]

[1]Physics Department, Gujarat University, Ahmedabad 380 009, India
[2]Space Applications Centre, Ahmedabad 380 015, India

Compact polarimetry has gained popularity due to its advantages, such as larger swath, simple architecture and low power consumption. The backscattered signal and scattering decomposition vary for different targets based on their electrical, geometrical and structural properties. As of now, the potential of hybrid polarimetric synthetic aperture radar (SAR) data for exploring Antarctic ice features is not fully explored. Here, we present a comprehensive polarimetric feature analysis and classification results of the hybrid polarimetric dataset acquired by RISAT-1 near the Indian Antarctic research station Maitri. The single-look complex images have been subjected to polarimetric data processing for extracting Antarctic ice features using POLSARPRO software. The polarimetric coherence matrix is generated and then filtered to eliminate speckles. Raney m–χ decomposition technique has been utilized to understand the scattering mechanism of the targets. The decomposed RGB image is classified using Wishart-supervised classification, and classification accuracy is assessed using a confusion matrix. It is found that the comparatively simple hybrid polarimetric SAR provides sufficient information to detect and discriminate various Antarctic ice features. Features such as rifts, ice–rises, ice shelves and icebergs are clearly discriminated using Wishart-supervised classification. It is also found that the overall accuracy of the classification of study areas varies between 80% and 97%, suggesting a good classification outcome.

Keywords: Classification accuracy, confusion matrix, hybrid polarimetry, ice features, m–χ decomposition, synthetic aperture radar data.

REMOTE sensing plays a vital role in monitoring various ice features, especially in polar regions where hostile climatic conditions and remoteness limit the availability of *in situ* data[1,2]. Microwave remote sensing is preferred over optical remote sensing for monitoring Antarctic ice features because it provides all-time and all-weather imaging capabilities and is independent of sun illumination conditions. Synthetic aperture radar (SAR), with its unique sensitivity to the geometrical, structural and electrical properties of the target, is an important tool for retrieving various ice features. Electromagnetic pulses from SAR interact differently with different types of ice depending upon feature characteristics such as surface roughness and dielectric constant, in addition to system characteristics such as wavelength and polarization. An important approach to feature extraction is the decomposition of data into a single (odd)-bounce scattering, double (even)-bounce scattering and volume scattering.

There are only limited studies on the identification of polar ice features using polarimetric data. Denbina and Collins[3] utilized compact polarimetry data for iceberg detection and proved that for higher incidence angles, the performance of compact polarimetry detectors is better than any dual-polarimetric detector, and it is comparable to quadrature polarimetric detectors. Dabboor and Geldsetzer[4] examined the potential of the compact polarimetry SAR system in the RADARSAT Constellation Mission satellites for sea-ice classification. Dabboor *et al.*[5] concluded that compact polarimetry SAR data from high-resolution SAR mode is promising for classifying first-year ice and multi-year ice in winter dry-ice conditions.

India has developed an agile spacecraft, viz. Radar Imaging Satellite-1 (RISAT-1), featuring a multi-mode and multi-polarization SAR system operating in the C-band (5.35 GHz)[6]. It provided spatial resolution in the range of 1–50 m and a swath ranging from 10 to 225 km and was launched on 26 April 2012 (ref. 6). RISAT-1 SAR operates in the hybrid polarimetry mode, where the signal is transmitted in circular polarization, and the backscattered signal is received simultaneously in H and V polarizations (RH and RV). In the present study, we demonstrate the potential of hybrid polarimetric SAR data near India Bay in Antarctica, acquired by RISAT-1, to extract Antarctic ice features by decomposing the SAR data into different scattering mechanisms and then classify the Antarctic ice features.

Study area and data used

RISAT-1 SAR has five different modes; the Fine Resolution Stripmap-1 (FRS-1) mode with 2.25 m spatial resolution and 25 km swath have been used in the present study. The study area covers the Indian Antarctic Research Station

*For correspondence. (e-mail: eshu7456@gmail.com)

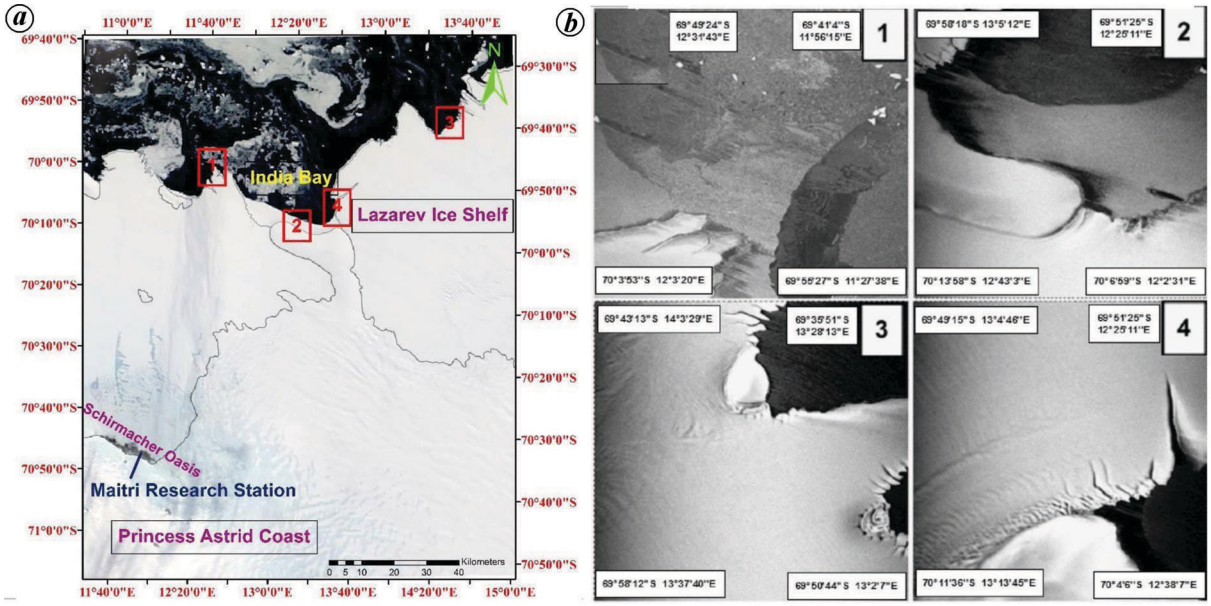

Figure 1. ***a***, MODIS image of the coastal region covering Indian Antarctic Research Station Maitri and the surroundings. ***b***, Selected study areas 1–4 over India Bay (Maitri coast) acquired by RISAT-1 FRS-1 (RH-polarization).

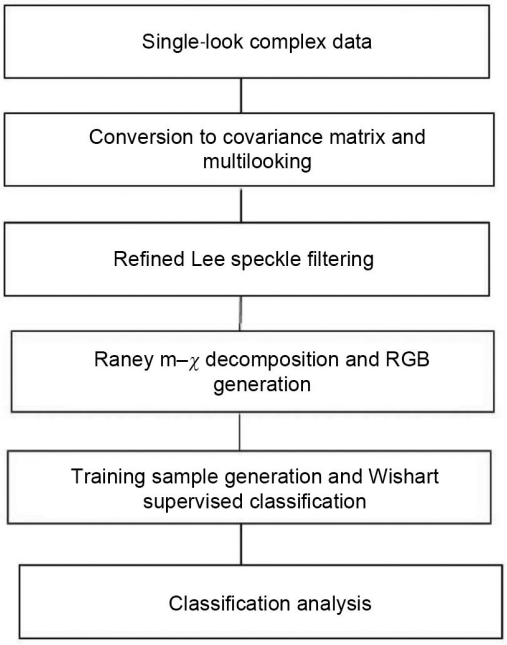

Figure 2. Flowchart of polarimetric SAR data processing.

Maitri (70°45′53″S, 11°44′03″E) located at Schirmacher Oasis and its surroundings on central Queen Maud Land in Antarctica. In the present study, four scenes have been selected for Antarctic ice-feature identification. Images of study areas 1 and 2 were acquired on 6 February 2015, with an incidence angle 34°. Images of study areas 3 and 4 were acquired on 2 March 2015 having an incidence angle 26°.

Figure 1 *a* shows the MODIS image of the coastal region covering Indian Antarctic Research Station Maitri and the surroundings (https://nsidc.org/data/iceshelves_images/cgi-bin/modis_iceshelf_archive.pl). Figure 1 *b* shows zoomed images of study areas 1–4 acquired on 2 March 2015 by RISAT-1. These study areas include different Antarctic ice features such as ice shelf, fast ice, ice rise, sea ice, water bodies, nilas, rifts, pancake ice, ice floe and iceberg.

Methodology

The downloaded single look complex (SLC) images in right-hand circular transmit and horizontal receive (RH) and Right-hand circular transmit and vertical receive (RV) were converted into a covariance matrix and subjected to multi-looking to reduce the slant range distortion. Using a refined Lee speckle filtering technique, noises were removed. Raney m–χ decomposition technique was applied, and RGB images based on odd, even and volume scattering of all four study areas were obtained. These RGB images were classified using the Wishart supervised classification technique. The classification accuracy of each image was evaluated using confusion matrices. The polarimetric data processing was carried out using POLSAR PRO V5.0.4 software. Figure 2 is a flowchart for hybrid polarimetric SAR data processing. Detailed concepts of hybrid polarimetric SAR data processing are discussed in the following sections.

Conversion of SLC data to covariance matrix

The RISAT-1 SLC images acquired in FRS-1 mode have been described in the form of the polarization state of an electromagnetic wave using amplitudes of E_{RH} and E_{RV} and the relative phase between them. According to Boerner[7],

the polarization state of a partially polarized wave in terms of 2×2 complex Hermitian positive semi-definite wave covariance matrix $[C]$ for RH and RV polarization can be expressed as follows

$$[C] = \langle EE^{\dagger} \rangle = \begin{bmatrix} \langle E_{\mathrm{RH}} E_{\mathrm{RH}}^{*} \rangle & \langle E_{\mathrm{RH}} E_{\mathrm{RV}}^{*} \rangle \\ \langle E_{\mathrm{RV}} E_{\mathrm{RH}}^{*} \rangle & \langle E_{\mathrm{RV}} E_{\mathrm{RV}}^{*} \rangle \end{bmatrix}, \quad (1)$$

where E is the electric field (in the subscripted polarization), $*$ denotes complex conjugate, † denotes complex conjugate transpose and $\langle \ldots \rangle$ indicates ensemble averaging (multi-looking in the context of SAR). To deal with a partially polarized wave, it is easier to use Stokes parameters as they describe partially polarized waves by their observable power terms instead of their phases and amplitudes[8]. The Stokes parameters for hybrid architecture can be expressed as follows[9]

$$g_0 = \langle |E_{\mathrm{RH}}|^2 \rangle + \langle |E_{\mathrm{RV}}|^2 \rangle,$$

$$g_1 = \langle |E_{\mathrm{RH}}|^2 \rangle - \langle |E_{\mathrm{RV}}|^2 \rangle,$$

$$g_2 = 2\,\mathrm{Re}(E_{\mathrm{RH}} E_{\mathrm{RV}}^{*}),$$

$$g_3 = -2\,\mathrm{Im}(E_{\mathrm{RH}} E_{\mathrm{RV}}^{*}). \quad (2)$$

For a completely polarized signal[10,11]

$$g_0^2 = g_1^2 + g_2^2 + g_3^2. \quad (3)$$

These Stokes parameters provide valuable information about the geophysical properties of the feature.

Multi-looking approach

The SAR data were generated in slant range geometry and must be projected into the ground range plane. Due to slant range distortion, earth objects in the near range appear more compressed than objects in the far range. Therefore, a multi-looking approach was used to convert the slant range into the ground range. For this, pixel spacing in the ground range was calculated by dividing pixel spacing in the slant range by the sine of the look angle (1.80 m and 260 respectively, for areas 3 and 4), which was 4.11 m. The multi-looking factor was obtained by comparing pixel spacing in the ground range with that in the azimuth range of 2.34 m. Here, two looks in the azimuth direction and one look in the range direction were considered to obtain square pixels. For study areas 1 and 2, the ground range evaluated was 3.21 m (pixel spacing 1.80 m and look angle 34°). Hence three looks in the azimuth direction and two looks in the range direction were considered to obtain square pixels.

Speckle filtering

The speckle in SAR images affects the correlation structure between the channels and the complex, cross-product terms of the covariance matrix. The refined Lee filter algorithm uses an edge-aligned window and applies local statistics to better preserve edges and spatial resolution details[12]. So, in the present study, a refined Lee filter was used for speckle removal of RISAT SAR images. This is an adaptive filter based on the estimation of the local variance statistics, and the filtering weights are determined using the span image. The filter does not use the standard square filtering window but an edge-aligned window to preserve edges and detailed features[13]. The edge direction was realized with the help of an edge mask using the sub-means of 3×3 sub-windows, which reduced the effect of noise in the edge direction and enhanced the weight of pixels within the proximity of the centre pixel. After filtering, each element of the covariance matrix C was decomposed using the m–χ decomposition method.

The m–χ decomposition technique

Raney *et al.*[14] proposed the m–χ decomposition technique for analysis of the hybrid polarimetric SAR data using Stokes classical and child parameters. The m–χ decomposition is achieved using three inputs: Stokes parameter g_0, degree of polarization (m) and ellipticity parameter (χ). The m–χ decomposition method facilitates the interpretation of features according to single-bounce, double-bounce and randomly polarized backscatter[14]. The decomposed elements can be represented in terms of double-bounce (dihedral reflectors), single-bounce (Bragg scattering) and volume component (a randomly polarized constituent) in the following form.

$$R = \text{Double bounce} = \sqrt{g_0 \times m \times \frac{1+\sin(2\chi)}{2}},$$

$$G = \text{Volume component} = \sqrt{g_0 \times (1-m)},$$

$$B = \text{Single bounce} = \sqrt{g_0 \times m \times \frac{1-\sin(2\chi)}{2}}. \quad (4)$$

Total power $g_0 = R^2 + C^2 + B^2$.

Based on this m–χ decomposition, an RGB colour composite was generated with R, G and B corresponding to even bounce scattering, volume scattering and odd bounce scattering respectively. The RGB colour composite of the decomposed image clearly suggests the scattering mechanisms

from different ice features. The intensity of each colour is given by the relative contribution of the scattering components. Black appearance in RGB indicates no backscattered energy, suggesting specular reflection from smooth surfaces such as water bodies. White patches in RGB indicate a combination of all three types of scattering, as in the case of icebergs. The secondary colours (cyan, magenta and yellow) represent a mix of scattering patterns. For example, magenta is a combination of double bounce and surface scattering.

Classification

In the present study, the decomposed hybrid polarimetric data (RGB image) were subjected to the Wishart supervised classification. Twelve distinct features, viz. ice shelf, snow-free ice shelf, fast ice, ice rise, rift, water bodies, sea ice 1 (smooth) and sea ice 2 (rough), nilas, pancake ice, ice floe and iceberg in the SAR images known with reasonable certainty based on experience gained by the scientific expedition were selected as training areas. The graphic interface application of PolSARpro software was used for defining training areas by visual interpretation of the images to be classified. The area of interest was selected from the m–χ decomposed RGB image. Using the Wishart statistics, the classifier learns from the user-defined training areas, and then the entire dataset is classified by assigning each pixel to the closest class using the maximum likelihood decision rule. The classification algorithm produces two different outputs; the classified image in .bmp format and the confusion matrix in .txt format.

Confusion matrix

The performance of the Wishart supervised classification was assessed using the confusion matrix computed by a set of sample data. The confusion matrix is a table that shows the correspondence between the classification result and a reference image. In the confusion matrix, rows represent the user-defined clusters (training class), and the columns represent the segmented clusters (classified or predicted class). The values at the ijth position in the matrix represent the percentage of pixels belonging to the user-defined area i assigned to cluster j during the Wishart supervised classification. Therefore, rows add up to 100%. The confusion matrix of an ideal, error-free classification should be diagonal, and the average of the diagonal gives the overall accuracy of classification. The off-diagonal elements in a confusion matrix represent misclassified pixels or classification errors.

Results and discussion

Figures 3–6 display the classified images of study areas 1–4 respectively, along with the original image and RGB of the m–χ decomposed image. The regions where single bounce, double bounce and volume scattering dominate are marked in Figures 3 *b*–6 *b* with blue, red and green boxes respectively. Major part of study area-1 (Figure 3) is covered by sea ice. The decomposed RGB image (Figure 3 *b*) clearly suggests that the sea-ice part is characterized by a combination of single and double bounce scattering. The top left part of the image is dominated by single surface scattering, while the top middle part shows nearly the same contribution by surface scattering and double bounce scattering. Sea ice-2 shows a higher double bounce compared to sea ice 1. This could be attributed to the fact that sea ice-1 is wet and smooth, giving rise to single scattering, whereas sea ice-2 is relatively thicker and rough compared to sea ice-1 and hence provide a higher double bounce signature.

Sea ice in area-2 (Figure 4 *b*) shows a darker appearance, suggesting that the surface is smoother and backscattered power is comparatively low. The absence of volume scattering clearly suggests that the sea ice in areas 1 and 2 is at its initial stage of formation.

Ice shelves were present in all the study areas. They consist of freshwater ice. Microwave radiation penetrates them, and volume scattering occurs due to multiple internal reflections from air bubbles, fractures and dust layers. Since ice shelves are thick in relation to radar wavelength, there may not be any return from the lower boundary between ice mass and water. A combination of predominantly volume scattering along with double-bounce scattering due to continuous accumulation of snow firns occurred over areas 1, 3 and 4. The left side of area 3 suggests the dominance of double-bounce scattering, suggesting the presence of more firns. In case of ice shelf over area 2, in addition to volume and double scattering, surface Bragg scattering due to surface roughness also contributed to backscattering. In case of ice shelf free from snow over areas 1 and 2, surface scattering and volume scattering mainly contributed to the backscattered power.

Since the structure of ice rises is similar to the ice shelf, the ice rises present in areas 2, 3 and 4 show similar characteristics of the ice shelf in decomposed images. The dominance of double and volume scattering over the surface Bragg scattering was observed over ice rises in areas 3 and 4. The boundary between ice rise and ice shelf was clearly visible in the decomposed image due to stronger double-bounce scattering caused by corner reflection along with volume scattering. Fast ice was present in all images. Fast ice at the top right part of area 3 and bottom right part of area 4 was clearly characterized by surface Bragg scattering, while for that in area 2, an additional small contribution by double-bounce scattering also occurred.

Over smooth water bodies, specular reflection causes less backscattering, resulting in a dark tone in the decomposed images (areas 1 and 2). Over the water bodies where nilas had developed (area 1), the presence of frost flowers or ice surface disturbed by rafting resulted in a combination of double-bounce scattering and surface scattering.

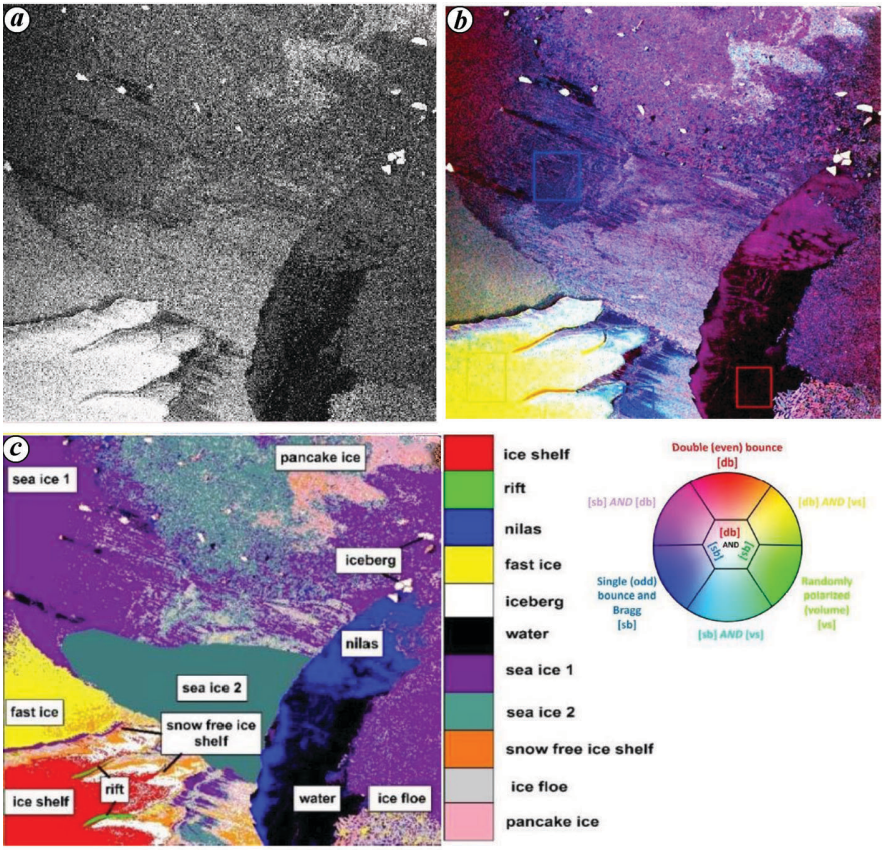

Figure 3. Study area-1: ***a***, Original SAR scene. ***b***, RGB of m–χ decomposed image. ***c***, Classified image.

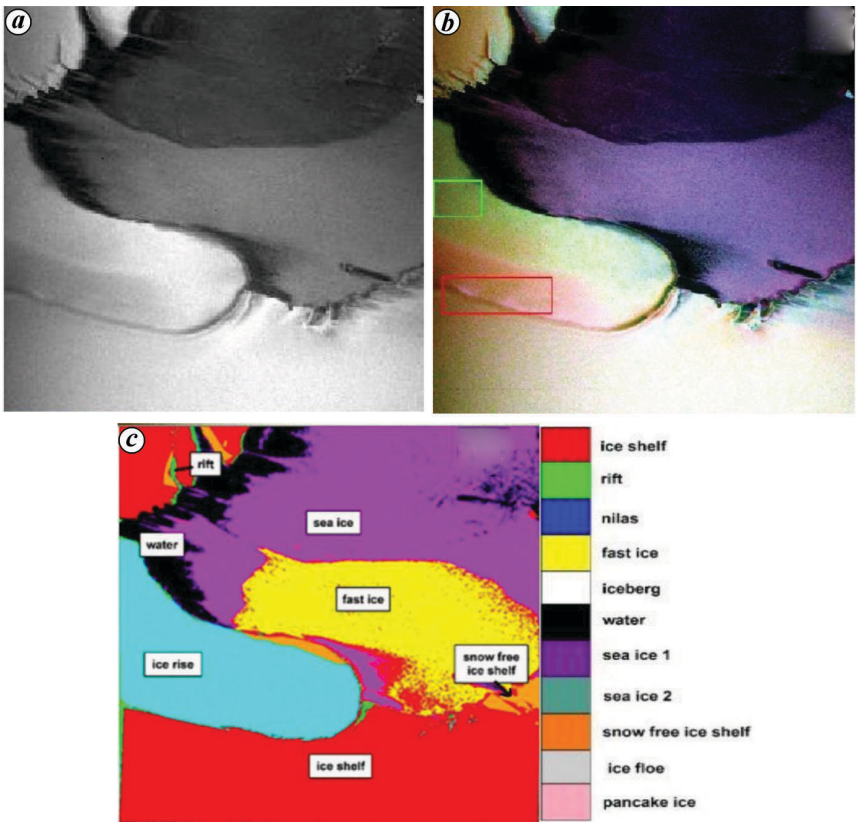

Figure 4. Study area-2: ***a***, Original SAR scene. ***b***, RGB of m–χ decomposed image. ***c***, Classified image.

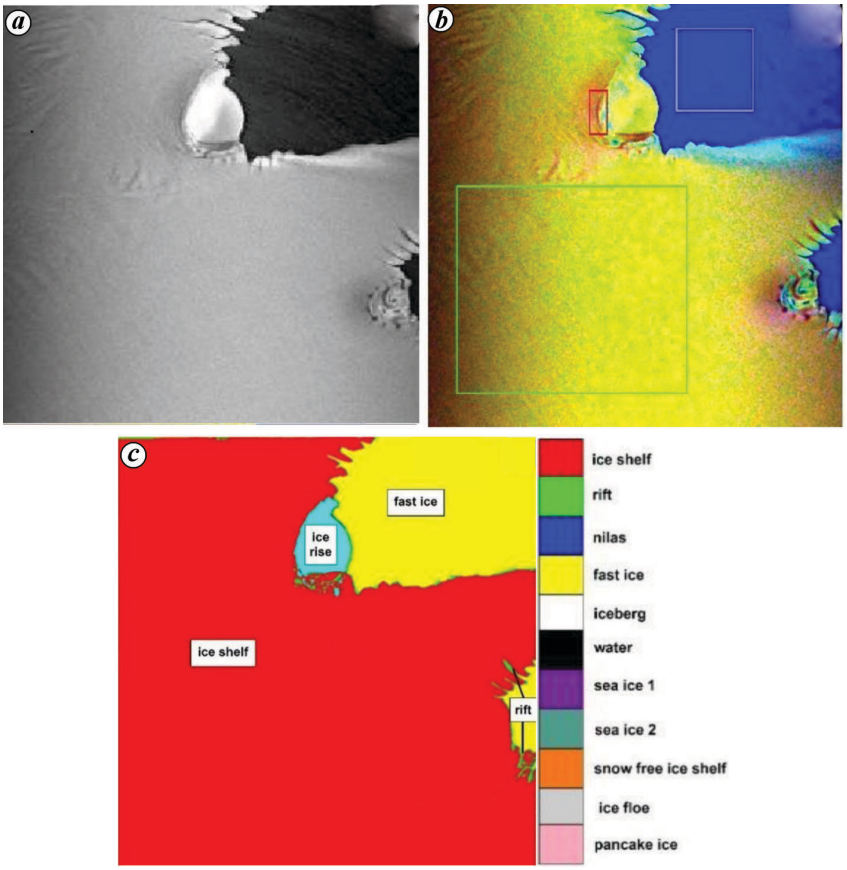

Figure 5. Study area-3: ***a***, Original SAR scene. ***b***, RGB of m–χ decomposed image. ***c***, Cassified image.

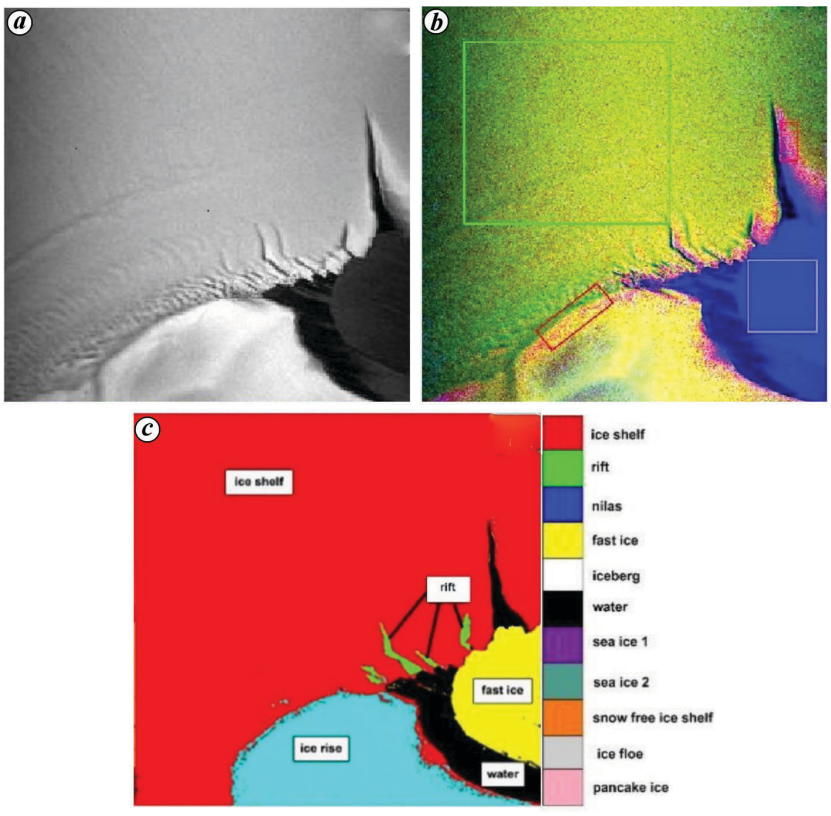

Figure 6. Study area-4: ***a***, Original SAR scene. ***b***, RGB of m–χ decomposed image. ***c***, Classified image.

Table 1. Confusion matrix for study area-1

	Predicted (classified) data										
User defined (training) data	Ice shelf	Rift	Nilas	Fast ice	Snow-free ice shelf	Water	Iceberg	Pancake ice	Ice floe	Sea ice 1	Sea ice 2
Ice shelf	92.94	0	0	0	0.19	0	6.87	0	0	0	0
Rift	0.15	99.85	0	0	0	0	0	0	0	0	0
Nilas	0	0	99.03	0.03	0	0.18	0	0	0.22	0.54	0
Fast ice	0	0.03	0	5.44	5.94	0	0.72	1.42	5.12	1.34	0
Snow-free ice shelf	1.12	0	0	0.97	49.91	0.23	26.87	13.85	4.12	1.24	1.70
Water	0	0	0.11	0	0	98.86	0	0	0	1.04	0
Iceberg	4.81	0.23	0	0.69	1.26	0	87.77	1.34	2.71	1.18	0
Pancake ice	0.69	0	0	1.31	15.70	0.09	12.06	49.93	16.37	1.11	2.75
Ice floe	0	0	1.44	2.40	2.09	0.21	0.56	9.70	48.73	21.05	3.82
Sea ice 1	0	0	0.03	0.02	0	0.09	0	0	1.88	97.77	0.21
Sea ice 2	0	0	0.21	0.01	0.04	0.01	0.05	1.62	16.45	8.35	73.26

Table 2. Confusion matrix for study area-2

	Predicted (classified) data						
User defined (training) data	Ice shelf	Snow-free ice shelf	Fast ice	Ice rise	Rift	Water	Sea ice 1
Ice shelf	96.07	0.04	3.88	0	0	0	0.01
Snow-free ice shelf	1.08	76.9	0.19	3.85	0.35	0	17.63
Fast ice	19.06	1.10	79.7	0	0	0	0.14
Ice rise	0	3.34	0	96.6	0	0	0.06
Rift	0	0	0.02	0	98.9	1.08	0
Water	0	0	0	0	0	100	0
Sea ice 1	0	8.93	0.88	0	0	0	90.19

Rifts were characterized by double-bounce scattering by dihedral structure at the rift wall and the surface with volume scattering. Heterogeneous combinations of single-bounce scattering, double-bounce scattering and volume scattering were observed over pancake ice and ice floe over area 1. Icebergs could be easily identified in the m–χ decomposed image as bright point targets with intensities much above that of the dark background of the ocean due to double-bounce scattering from natural dihedrals on icebergs along with surface scattering and volume scattering.

Figures 3 *c*, 4 *c*, 5 *c* and 6 *c* show classified images of study areas 1, 2, 3 and 4 respectively, based on the Wishart supervised classification technique. The study areas were classified into 12 distinct groups, viz. ice shelf, snow-free ice shelf, fast ice, ice rise, rift, water bodies, sea ice 1 (smooth) and sea ice 2 (rough), nilas, pancake ice, ice floe and iceberg. Each class was discriminated by unique colours. Quantitative assessment of the classification accuracy of all images was done using confusion matrices (Tables 1–4).

As seen in Figure 3 *c*, area-1 consists of 11 different classes. In the classified image, features like water body, rift, nilas, sea ice 1, ice shelf and icebergs are clearly discriminated. Snow-free ice shelf is not clearly discriminated in the decomposed image but is separated in the classified images. The confusion matrix also suggests that features such as water body, rift, nilas and sea ice-1 are well discriminated with class accuracy of more than 97% (Table 1). Both the image as well as confusion matrix suggest that features such as pancake ice, ice floe and snow-free ice shelf are not clearly discriminated. More than 50% of the pixels of pancake ice, ice floe and snow-free ice shelf are classified as other groups. The overall classification accuracy of area-1 is found to be 80.3%.

Study area-2 is classified into seven features: ice shelf, sea ice, fast ice, rift, snow-free ice shelf, water, and ice rise (Figure 4 *c*). The decomposed image shows similar characteristics between ice shelf and ice rise, but the classified image clearly distinguishes between them. Similarly, rifts are not clearly distinguishable from the boundary between the ice shelf and ice rise in the decomposed image, but the classified image shows a clear distinction. Snow-free ice shelf is clearly separated from the ice shelf. Water body, sea ice and fast ice, are well discriminated. The overall classification accuracy of area-2 is 91.2%. Features like water body, rift, ice rise and ice shelf have been precisely classified with an accuracy of more than 96%.

Study area-3 is classified into four groups, viz. ice shelf, ice rise, sea ice and rifts (Figure 5). In this area, all features are well separated. The overall classification accuracy of this scene is 97.3%. Class accuracy of fast ice, rift and ice rise is more than 96%. Area-4 has been classified into five classes, viz. ice shelf, water, rift, fast ice and ice rise. The overall classification accuracy of this scene is 95.3%. Water,

Table 3. Confusion matrix for study area-3

	Predicted (classified) data			
User defined (training) data	Ice shelf	Ice rise	Fast ice	Rift
Ice shelf	93.16	6.84	0	0
Ice rise	3.74	96.26	0	0
Fast ice	0	0	100	0
Rift	0.40	0	0	99.60

Table 4. Confusion matrix for study area-4

	Predicted (classified) data				
User defined (training) data	Ice shelf	Ice rise	Fast ice	Rift	Water
Ice shelf	91.96	8.04	0	0	0
Ice rise	12.23	87.77	0	0	0
Fast ice	0	0	99.69	0.31	0
Rift	0	0	2.09	97.08	0.83
Water	0.16	0	0	0	99.84

fast ice and rift have a class accuracy of more than 97%. The confusion matrix shows that ice rise and ice shelf get merged with each other. The most conspicuous feature of these images is the clear identification of a rift on the ice shelf. Comparison of decomposed RGB images and the corresponding classified images show good matching, and most of the features are well discriminated. Among the 12 classified features, water, rift and nilas have excellent accuracy of more than 97%. Sea-ice features like pancake ice and ice floe are inefficiently classified. Overall classification accuracy of all four study areas is comparatively good: above 90%. Study area-3, which has only four classes, shows the best overall classification accuracy of more than 97% and study area-1 with 11 classes shows comparatively low overall accuracy (80%). In comparison with the decomposed images, features such as snow-free ice shelf and rifts are well discriminated, and the boundary between the ice shelf and ice rise becomes clear.

Conclusion

In this study, we have examined the capability of hybrid polarimetric data retrieved from RISAT-1 of ISRO to understand the scattering response of various Antarctic ice features. The m–χ decomposition technique based on Stokes parameters has been used to separate the backscattered signal into surface, volume and double-bounce components which are useful indicators of the physical properties of Antarctic surface features. Polarimetric SAR data analysis has shown the potential for discriminating various ice features such as ice shelf, fast ice, water, sea ice, rift, nilas, snow-free ice shelf and icebergs over Antarctica. The decomposed RGB images are classified based on Wishart classifier, and the overall classification accuracy of the study areas varies between 80% and 97%, suggesting a satisfactory classification. Thus, from this study, it can be concluded that the hybrid polarimetric SAR data from RISAT-1 provide sufficient information about scattering mechanisms, which helps in extracting various Antarctic ice features. The overall accuracy of classification can be improved by a sound knowledge of the ground-truth information. Future studies may consider other features of Antarctica, possibly with simultaneous *in situ* data for validation.

1. Clausi, D. A. and Deng, H., Operational segmentation and classification of SAR sea ice imagery. In Proceedings of IEEE Workshop on Advances in Techniques for Analysis of Remotely Sensed Data, Greenbelt, MD, USA, 2003, pp. 268–275.
2. Moen, M. A., Doulgeris, A. P., Anfinsen, S. N., Renner, A. H., Hughes, N., Gerland, S. and Eltoft, T., Comparison of feature based segmentation of full polarimetric SAR satellite sea ice images with manually drawn ice charts. *Cryosphere*, 2013, **7**, 1693–1705.
3. Denbina, M. and Collins, M. J., Iceberg detection using simulated dual-polarized Radarsat constellation data. *Can. J. Remote Sensing*, 2014, **40**, 165–178.
4. Dabboor, M. and Geldsetzer, T., On the classification of sea ice types using simulated Radarsat Constellation Mission (RCM) compact polarimetric SAR parameters. In Proceedings of the ASPRS 2014 Annual Conference, Louisville, Kentucky, USA, 2014, pp. 23–28.
5. Dabboor, M., Montpetit, B. and Howell, S., Assessment of the high resolution SAR mode of the RADARSAT Constellation Mission for first year ice and multiyear ice characterization. *Remote Sensing*, 2018, **10**, 594.
6. Misra, T., Rana, S. S., Desai, N. M., Dave, D. B., Rajeevjyoti, Arora, R. K. and Vachchani, J. G., Synthetic aperture radar payload on-board RISAT-1: configuration, technology and performance. *Curr. Sci.*, 2013, **104**, 446–461.
7. Boerner, W. M., Basic concepts in radar polarimetry (on-line); available at http://envisat.esa.int/polsarpro/Manuals/LN_Basic_Concepts.pdf
8. Tomar, K. S., Hybrid polarimetric decomposition for aboveground biomass estimation using semi-empirical modelling. MS thesis submitted to the University of Twente, The Netherlands, 2015, p. 70.
9. Sabry, R. and Vachon, P. W., Advanced polarimetric synthetic aperture radar (SAR) and electro-optical (EO) data fusion through unified coherent formulation of the scattered EM field. *Prog. Electromagn. Res.*, 2008, **84**, 189–203.

10. Woodhouse, I. H., *Introduction to Microwave Remote Sensing*, CRC Press, FL, Boca Raton, USA 2006, p. 370.
11. Raney, R. K., Synthetic aperture radar hybrid-quadrature-polarity method and architecture for obtaining the stokes parameters of radar backscatter. US Patent 8,258,996, 2012.
12. Lee, J. S., Grunes, M. R. and De Grandi, G., Polarimetric SAR speckle filtering and its implication for classification. *IEEE Trans. Geosci. Remote Sensing*, 1999, **37**, 2363–2373.
13. Farage, G., Foucher, S. and Benie, G., Comparison of PolSAR speckle filtering techniques. In Proceedings of 2006 IEEE International Symposium on Geoscience and Remote Sensing, Denver, CO, USA, 2006, pp. 1760–1763.
14. Raney, R. K., Cahill, J. T., Patterson, G. W. and Bussey, D. B. J., The *m*–chi decomposition of hybrid dual-polarimetric radar data with application to lunar craters. *J. Geophys. Res. Planets*, 2012, **117**, 8.

ACKNOWLEDGEMENTS. We thank the Director and Deputy Director Earth, Ocean, Atmosphere, Planetary Sciences and Applications Area, Space Applications Centre (SAC), Ahmedabad for providing the opportunity to work in collaboration with Gujarat University. We also thank the Head and colleagues at the Cryosphere Science Division, SAC, the Head, Microwave Data Processing Division and the Head, Physics Department, Gujarat University for support. Financial support extended to the Physics Department, Gujarat University by University Grants Commission and Department of Science and Technology through Special Assistance Programme and fund for improvement of S&T infrastructure programmes respectively, is acknowledged.

Received 19 September 2022; revised accepted 20 February 2023

doi: 10.18520/cs/v124/i12/1445-1453